Journal of Atmospheric and Solar-Terrestrial Physics 71 (2009) 1126–1144

Contents lists available at ScienceDirect

Journal of Atmospheric and Solar-Terrestrial Physics

journal homepage: www.elsevier.com/locate/jastp

Relativistic electron losses related to EMIC waves during CIR and CME storms

M.I. Sandanger [a,*], F. Søraas [a], M. Sørbø [a], K. Aarsnes [a], K. Oksavik [b], D.S. Evans [c]

[a] Department of Physics and Technology, University of Bergen, Allégt 55, N-5007 Bergen, Norway
[b] The University Centre in Svalbard, PB 156, N-9171 Longyearbyen, Norway
[c] NOAA Space Environment Center, 325 Broadway, Boulder, CO 80305, USA

ARTICLE INFO

Article history:
Accepted 14 July 2008
Available online 30 July 2008

PACS:
94.30.Lr
94.30.cb
94.30.Xy
94.30.cv
94.20.wj
94.30.Ny

Keywords:
Relativistic electrons
EMIC waves
High-speed streams
Protons

ABSTRACT

The losses of radiation belt electrons to the atmosphere due to wave–particle interactions with electromagnetic ion-cyclotron (EMIC) waves during corotating interaction region (CIR) storms compared to coronal mass ejections (CME) storms is investigated. Geomagnetic storms with extended 'recovery' phases due to large-amplitude Alfvén waves in the solar wind are associated with relativistic electron flux enhancements in the outer radiation belt. The corotating solar wind streams following a CIR in the solar wind contain large-amplitude Alfvén waves, but also some CME storms with high-speed solar wind can have large-amplitude Alfvén waves and extended 'recovery' phases. During both CIR and CME storms the ring current protons are enhanced. In the anisotropic proton zone the protons are unstable for EMIC wave growth. Atmospheric losses of relativistic electrons due to weak to moderate pitch angle scattering by EMIC waves is observed inside the whole anisotropic proton zone. During storms with extended 'recovery' phases we observe higher atmospheric loss of relativistic electrons than in storms with fast recovery phases. As the EMIC waves exist in storms with both extended and short recovery phases, the increased loss of relativistic electrons reflects the enhanced source of relativistic electrons in the radiation belt during extended recovery phase storms. The region with the most unstable protons and intense EMIC wave generation, seen as a narrow spike in the proton precipitation, is spatially coincident with the largest loss of relativistic electrons. This region can be observed at all MLTs and is closely connected with the spatial shape of the plasmapause as revealed by simultaneous observations by the IMAGE and the NOAA spacecraft. The observations in and near the atmospheric loss cone show that the CIR and CME storms with extended 'recovery' phases produce high atmospheric losses of relativistic electrons, as these storms accelerate electrons to relativistic energies. The CME storm with short recovery phase gives low losses of relativistic electrons due to a reduced level of relativistic electrons in the radiation belt.

1. Introduction

The dynamics of relativistic electrons in the inner magnetosphere have received considerable attention in recent years. The scientific issues related to the transport, acceleration and loss of these particles pose a number of interesting questions that have not yet been resolved. For a review of relativistic electron dynamics in the inner magnetosphere, see Friedel et al. (2002).

Reeves et al. (2003) found that geomagnetic storms can either increase or decrease the fluxes of relativistic electrons in the radiation belts. About half of the geomagnetic storms increased the fluxes; about one in five storms decreased the fluxes; and the remaining storms produced changes that

* Corresponding author. Tel.: +47 906 900 94.
E-mail address: Marit.Sandanger@ift.uib.no (M.I. Sandanger).

1364-6826/$ - see front matter © 2008 Elsevier Ltd. All rights reserved.
doi:10.1016/j.jastp.2008.07.006

were less than a factor of two either up or down. They also found that equally intense post-storm fluxes can be produced out of nearly any pre-existing population. The results of Reeves et al. (2003) highlight the importance of relativistic electron losses during geomagnetic storms. The losses (Reeves et al., 2003) discussed are not temporary, adiabatic responses (the 'Dst effect') but real losses of electrons to the magnetopause or to the ionosphere as they compare pre-storm levels of relativistic electrons to post-storm levels. They also found that higher solar wind velocities increase the probability of an increase in the relativistic electron flux. But for all solar wind velocities both increases and decreases were still observed (Reeves et al., 2003).

During the rising and maximum phases of solar cycles the coronal mass ejections (CME) magnetic storms dominate and during the declining and minimum phases of solar cycles the corotating interaction region (CIR) magnetic storms occur more often (Gonzalez et al., 2007). (See Borovsky and Denton, 2006, for the major differences and comparisons between CME and CIR storms.) CIRs are created when solar wind fast streams emanating from solar coronal holes interact with upstream slow streams. The high-speed solar wind contains large-amplitude Alfvén waves (Tsurutani et al., 1994). In the interplanetary magnetic field (IMF) this appears as a rapid variation in the B_z (north–south) component, which leads to intermittent bursts of reconnection with the Earth's magnetic field and continuous auroral activity. Some of these geomagnetic disturbances have earlier been called high-intensity long-duration continuous AE-activity or HILDCAA (Tsurutani and Gonzalez, 1987; Tsurutani et al., 1990, 1999, 2004). HILDCAA events were defined by Tsurutani and Gonzalez (1987) as intervals where (1) AE peak values exceed 1000 nT, (2) the duration is greater than 2 days and (3) the AE values never drops below 200 nT for more than 2 h at a time. (4) The HILDCAA period must be separate from magnetic storm main phases. These criteria are relatively strict, and events that do not satisfy all the criteria rigorously may nevertheless be HILDCAA-like in physical characteristics.

The relatively short-duration reconnection at the magnetopause will produce minor injections of protons into the nightside magnetosphere (Søraas et al., 2004; Sandanger et al., 2005). Søraas et al. (1999) have shown that the isotropic proton precipitation on the nightside is a measure of the injected energy into the ring current, as the protons have an isotropic pitch angle distribution during injection. During HILDCAA events the ring current loss rate is balanced by injection of particles into the outer part of the ring current. These repetitive small injections of 'fresh' protons can keep the Dst depressed for days and give a long 'recovery' phase which is characteristic for CIR storms and HILDCAAs.

HILDCAA events and extended 'recovery' phases can occur after CME storms as well as after CIR storms (Guarnieri et al., 2006; Tsurutani et al., 2006). Some CME magnetic storms with high-speed solar wind intervals can have large-amplitude Alfvén waves, much like those in corotating solar wind streams. However, most of the HILDCAA events and extended 'recovery' phases occur after CIR storms, when the occurrence of Alfvén waves is more frequent (Guarnieri et al., 2006). Tsurutani et al. (2004) showed that the auroral intensifications during HILDCAAs are not substorm expansion events, nor convection bay events, thus giving us a new form of geomagnetic and auroral activity, see also Tsurutani and Gonzalez (2007).

One important aspect of HILDCAA/CIR events is the acceleration of relativistic electrons. Miyoshi and Kataoka (2005) have compared CME storms and CIR storms and found that CIR storms will cause a stronger enhancement of radiation belt electrons during the recovery phase due to the fast solar wind stream that always follows the CIR. Acceleration of relativistic electrons occurs during high-speed streams/HILDCAAs but the exact mechanism for energization is debated at this time (Tsurutani et al., 2006). The two classes of theories for acceleration both involve plasma waves. In this paper we will focus on loss of relativistic electrons to the atmosphere and will therefore only give a short overview of the theories of acceleration mechanisms.

Baker et al. (1998a, b) suggested that the production of relativistic electrons requires two ingredients: a 'seed' population of 100–200 keV electrons in the outer magnetosphere and a long-duration, powerful occurrence of ULF waves in the PC4–5 frequency range. The electrons experience radial diffusion within the magnetosphere due to the long-period magnetic oscillations (PC5) that break the particles third adiabatic invariant (O'Brien et al., 2001; Mann et al., 2004; Miyoshi et al., 2004). The second mechanism is energy diffusion by cyclotron resonant interactions with electromagnetic whistler mode waves called chorus (Summers et al., 1998, 2004; Horne and Thorne, 1998; Meredith et al., 2003a). This interaction breaks the particles' first adiabatic invariant.

Summers et al. (2004) modeled energetic electron fluxes at $L = 5$ during three events using wave and particle data from the combined release and radiation effects spacecraft (CRRES). They observed energetic electron flux enhancements during the recovery phase, when there was prolonged substorm activity, as measured by AE, and associated enhanced chorus waves. On this basis, they expected that HILDCAA events, during which prolonged substorms and enhanced chorus activity occur, will be associated with relativistic electron enhancements in the outer radiation belts. The prolonged substorm activity (that gives us a prolonged recovery phase) produces enhanced whistler mode chorus and electromagnetic ion-cyclotron (EMIC) waves. The whistler mode chorus will accelerate electrons to relativistic energies while EMIC waves will scatter the particles into the atmospheric loss cone (Summers et al., 1998, 2004, 2007a, b; Summers and Ma, 2000; Sandanger et al., 2007).

Sandanger et al. (2007) investigated atmospheric loss of relativistic electrons during geomagnetic storms. They found that this loss took place inside the anisotropic proton zone. In this zone the proton population is unstable and can give rise to the growth of EMIC waves. They also found localized peaks of enhanced proton precipitation, or spikes, directly related to increased precipitation of relativistic electrons. Lundblad and Søraas (1978) were the

first to observe such spikes in the protons using ESRO I observations. They found that the spikes were directly related to SAR (subauroral red) arc and suggested that these spikes were evidence of an unstable proton population which generated EMIC waves. Through Landau interaction these waves gave rise to SAR arc supporting the theory by Cornwall et al. (1971). Søraas et al. (1999) further substantiated that the proton spikes were associated with SAR arcs.

Yahnina et al. (2000) investigated localized bursts of both precipitating and locally trapped >30 keV protons within the anisotropic proton zone. They found these localized precipitation spikes, both the isotropic ones, observed with equal intensity both along and normal to the magnetic field and the anisotropic ones, observed normal to the magnetic field, were connected to Pc1 pulsations on the ground. They argued this to be due to the ion-cyclotron instability of energetic ring current protons (Yahnina et al., 2000, 2002, 2003). Yahnin et al. (2007) confirmed the EMIC instability to be the source of the subauroral proton aurora due to the close connection between the proton aurora spots and the Pc1 pulsations. They concluded that the Pc1 source is localized both in latitude and longitude, and they associated the Pc1 source with an azimuthal gradient of the cold plasma that appears due to a ripple at the plasmapause.

Our aim in the present investigation is to extend the Sandanger et al. (2007) study and investigate the loss of ring current ions and relativistic electrons to the atmosphere during CIR and CME storms. We focus on three major geomagnetic storms. The first is a CIR storm, the other two are both CME storms, but one of them exhibits a long 'recovery' phase associated with Alfvén waves in the solar wind, while the other has a short recovery phase.

2. Spacecraft instrumentation

We will use particle data from the low altitude polar orbiting NOAA 12, NOAA 14 and NOAA 15 spacecraft. From the NOAA 14 spacecraft we will only use particle data from the dome detectors since the telescopes never functioned properly. The NOAA spacecraft orbit the Earth with a Sun-synchronous circular orbit at an altitude of about 815 km. The orbital period is around 103 min. Footprints of the NOAA 12, NOAA 14 and NOAA 15 for the year 1998 are displayed in Fig. 1.

The space environment monitor (SEM-1) onboard the NOAA 12 and NOAA 14 spacecraft differs in energy range from the SEM-2 onboard the newer spacecraft NOAA 15.

2.1. SEM-1 onboard NOAA 12 and NOAA 14

The MEPED instrument consists of two identical proton telescopes and two identical electron telescopes with opening angle of 15° (half-angle). A pair of proton and electron telescopes is mounted to view outward along the Earth-center-to-satellite direction (termed 0° telescopes). The other pair of proton and electron telescopes is mounted to view normal to the first pair of telescopes and normal to the direction of the spacecraft velocity (termed 90° telescopes).

The MEPED instrument also contains three omnidirectional proton detectors (see Table 1). The first of these detectors is behind a 1.23 mm Al absorber, preventing electrons below 600 keV and protons <15 MeV to enter the detector. Relativistic electrons would, however, penetrate the shielding of the dome and give up a small amount of energy in the detector. The electronic trigger level in SEM-1 dome detector is set to 200 keV. Taking into

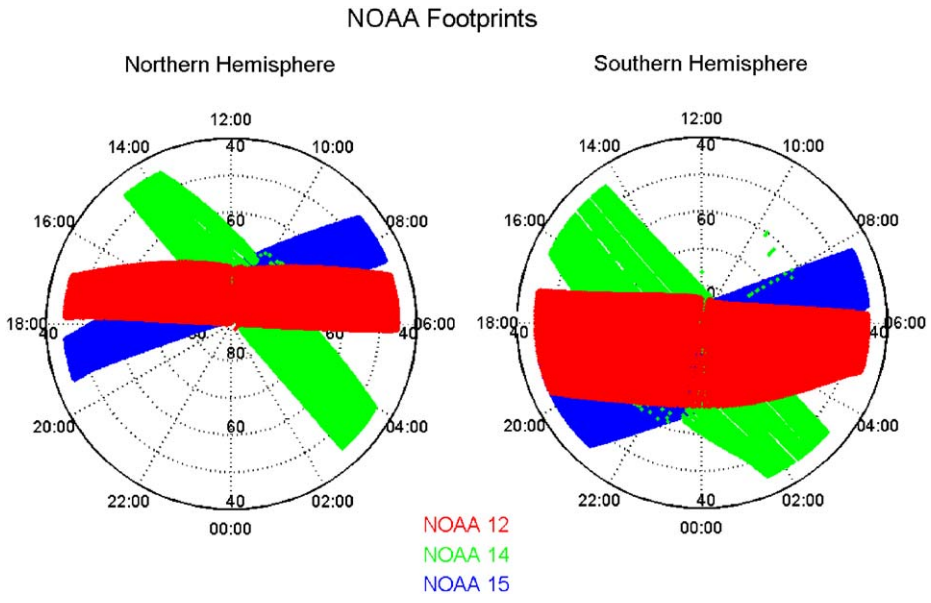

Fig. 1. The footprints of NOAA 12, 14 and 15 orbits in 1998, plotted against MLT and invariant latitude. Southern Hemisphere to the left, and Northern Hemisphere to the right.

account the shielding and the electronic trigger level, the detector will respond to electrons with energies >800 keV. The response function (efficiency) of the detector reaches a value of around 0.5 at around 1.5 MeV. T. Cayton (private communication, 2003) has evaluated the energy dependent sensitivity of the detector to electrons, and his results are used in the present work. Due to the dome detector's large geometric factor to high energy electrons, the NOAA 12 and NOAA 14 spacecraft give unique opportunities to detect relativistic electrons with energies >1.0 MeV near and within the atmospheric loss cone. Fortunately enough >16 MeV protons have a quite different characteristic than >1.0 MeV electrons (see Fig. 2) and 'contaminate' the relativistic electron measurements only at solar proton events. A full description of the NOAA 12 spacecraft and its instrumentation is given by Raben et al. (1995).

In the L range 3–7 the atmospheric loss cone at the spacecraft altitude is $59.4 \pm 0.5^{\circ}$, assuming that the particles are lost at 110 km altitude. See Table 2 for the detectors opening angles and observing directions with respect to the local magnetic field line at Northern Hemisphere in the L range 3–7. When the spacecraft is at high latitudes, the horizontal detector will measure particles just outside the loss cone, and the vertical detector will measure in the central part of the loss cone. The opening angle of the dome instrument is almost equal to the loss cone, and measures particles that are mostly inside the loss cone.

2.2. SEM-2 onboard NOAA 15

In the NOAA spacecraft launched after 1997 carry a modified sensor called SEM-2. The 90° electron and

Table 1
List of the energy channels for the SEM-1 omnidirectional proton detectors

	Looking direction	Opening angle	Proton energy (MeV)	Response to electron energy (MeV)
D1	Radial	±60°	>16	>1.0
D2	Radial	±60°	>36	
D3	Radial	±60°	>80	

Table 2
List of the observing directions with respect to the local magnetic field in the L range 3–7 for the telescope and omnidirectional detectors in SEM-1

Detector	Opening angle	Observing direction
Horizontal	±15°	88.5–90.5°
Vertical	±15°	10.8–19.9°
Omnidirectional	±60°	10.8–19.9°

Table 3
List of the energy channels for the SEM-2 omnidirectional proton detectors

	Looking direction	Opening angle	Proton energy (MeV)	Response to electron energy (MeV)
D1	Radial	±60°	>16	>3
D2	Radial	±60°	>35	
D3	Radial	±60°	>70	
D4	Radial	±60°	>140	

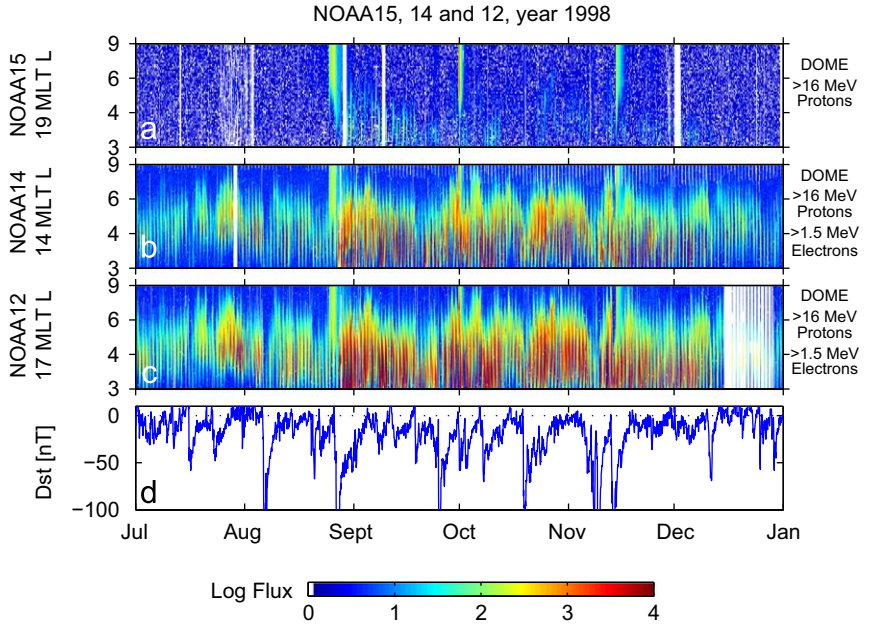

Fig. 2. Simultaneous data from the dome detector at NOAA 15, NOAA 14 and NOAA 12 spacecraft for the last six last months of 1998. The dome onboard NOAA 15 (panel (a)) detects only >16 MeV protons, while the dome onboard NOAA 14 (panel (b)) and NOAA 12 (panel (c)) detects >1.0 MeV electrons as well due to different electronic trigger levels. The fluxes are shown with a logarithmic color scale, plotted versus L and time. Panel (d) displays the Dst index.

proton telescopes in SEM-2 differ from SEM-1 in viewing direction. The SEM-2 pair of 90° telescopes is mounted normal to the pair of 0° telescopes as in SEM-1, but antiparallel to the direction of the spacecraft velocity.

The electron telescopes in SEM-2 have the same integral channels as in SEM-1. The two proton telescopes in SEM-2 have one more differential channel than SEM-1, and the integral channel measures much higher energies than in SEM-1. On SEM-2 the integral channel can monitor

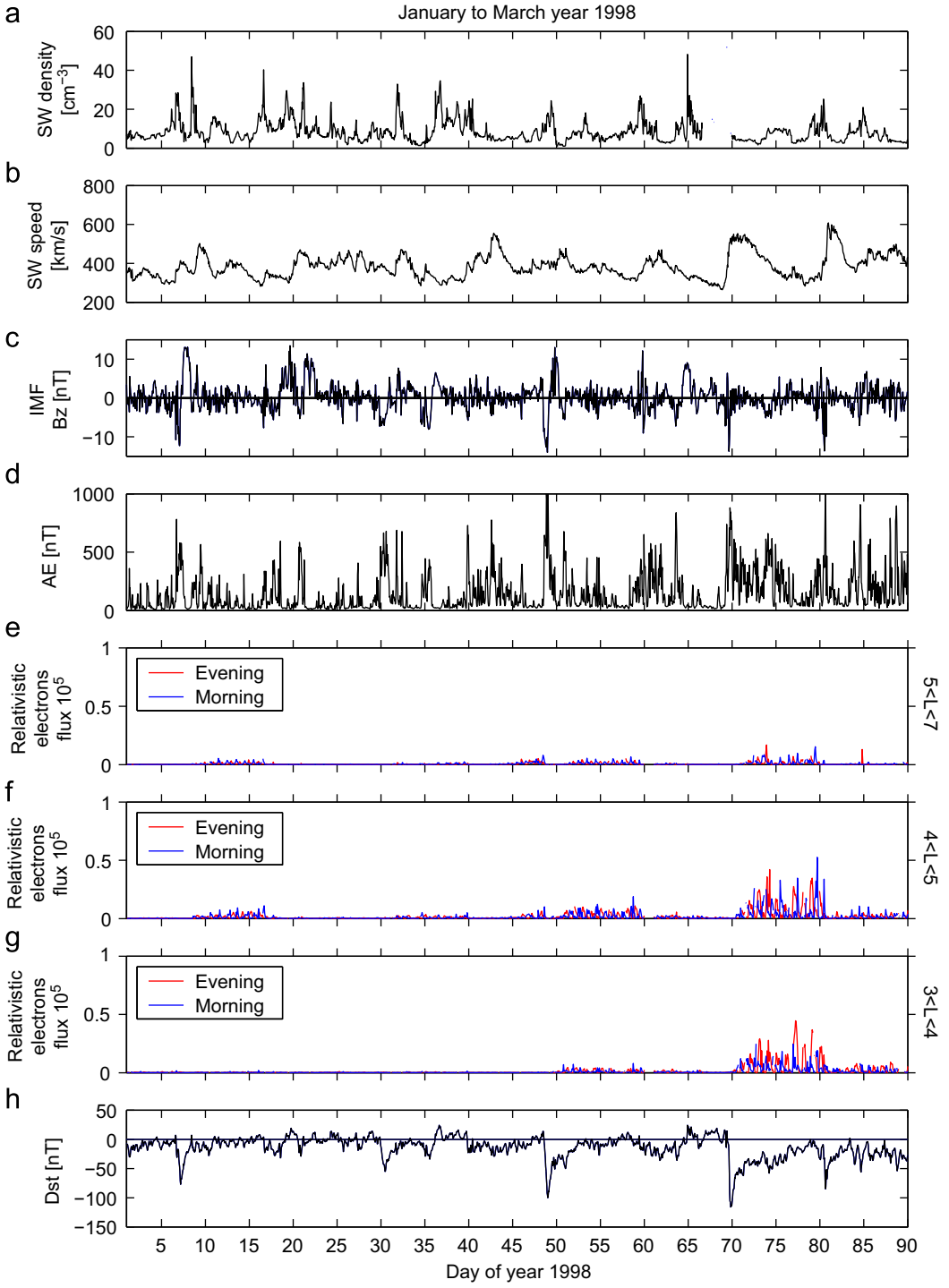

Fig. 3. Solar wind and NOAA 12 particle data from January to March, 1998. Panels (a) and (b) display solar wind density and speed. Panels (c) and (d) display IMF B_z and the AE index. Panels (e)–(g) exhibit electrons >1.0 MeV sorted into three L regions. Relativistic electrons detected in the evening sector are plotted in red, while data from the morning sector are plotted in blue. Panel (h) displays the Dst index. For colour, please see the web.

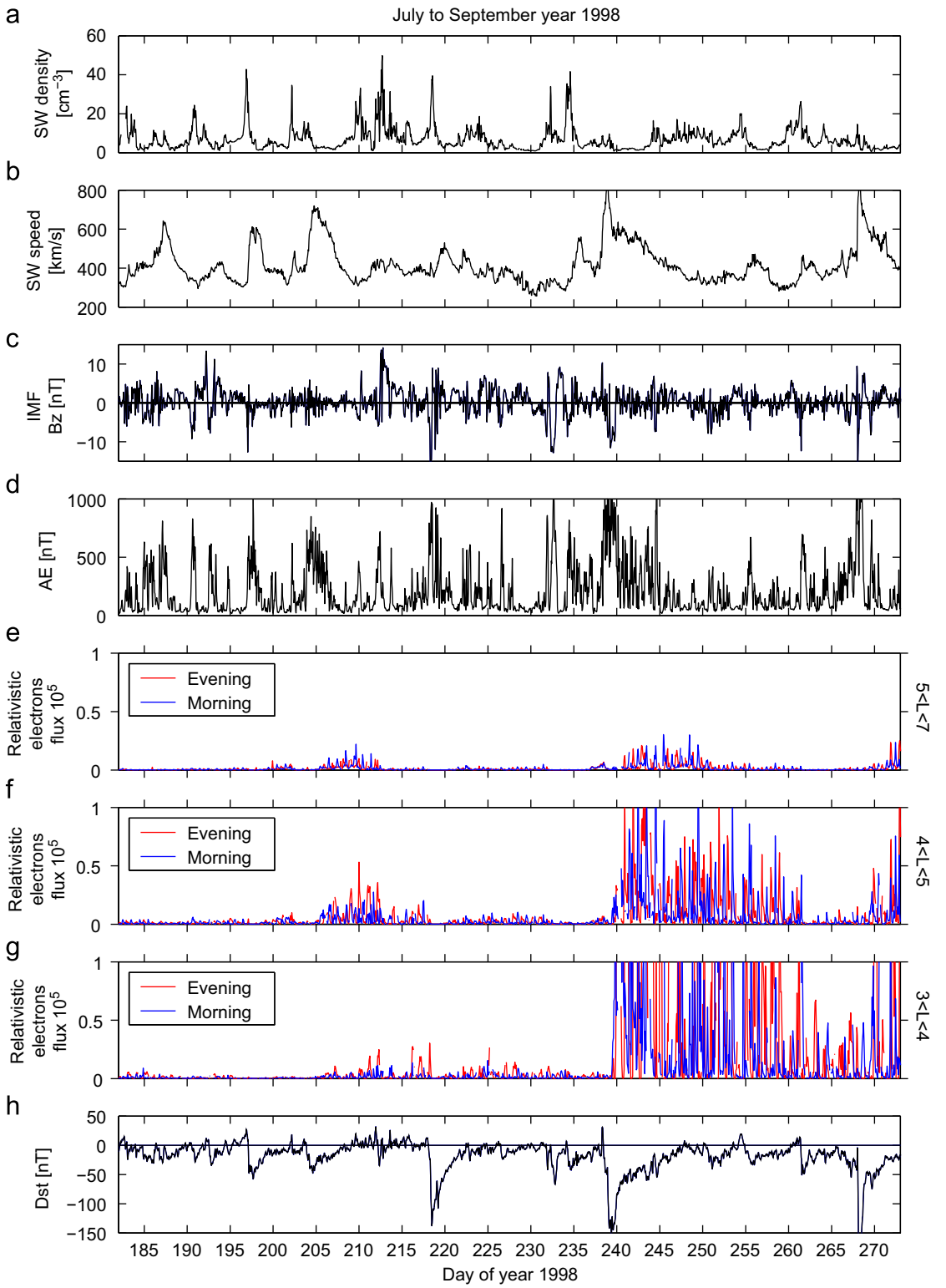

Fig. 4. Solar wind and NOAA 12 particle data from July to September, 1998. Panels (a) and (b) display solar wind density and speed. Panels (c) and (d) display IMF B_z and the AE index. Panels (e)–(g) exhibit electrons >1.0 MeV sorted into three L regions. Relativistic electrons in the evening sector are plotted in red, while data from the morning sector are plotted in blue. Panel (h) displays the Dst index. For colour, please see the web.

>1 MeV electrons because the sweeping magnet is not very effective at those high electron energies.

The SEM-2 MEPED instrument consists of four omni-directional proton detectors (see Table 3). They have the same opening angle and viewing direction as the dome detectors in SEM-1, but in SEM-2 the electronic trigger level is raised, thus making the detector respond to electrons >3 MeV. A full description of the newer NOAA spacecraft and their SEM-2 instrumentation is given by Evans and Greer (2000).

2.3. *In situ verification of SEM-1 and SEM-2 response to relativistic electrons*

In Fig. 2 we show simultaneous data from the three spacecraft at different magnetic local times during 1998. Panel (a) displays measurements from the dome instrument onboard NOAA 15, which detects >16 MeV protons. This detector is less sensitive to relativistic electrons. Panels (b) and (c) show measurements from the dome instrument onboard NOAA 14 and NOAA 12. These instruments detect electrons >1.0 MeV as well as protons >16 MeV. There are three solar proton events shown in Fig. 2. One event in the very end of August, one at the beginning of October and the one in the middle of November. The solar proton events are visible in data from all three spacecraft, while the relativistic electrons are only visible in NOAA 12 and NOAA 14. It is seen that there is a close association between the loss of relativistic electrons and geomagnetic disturbance level as given by the Dst index.

3. On the relation between the solar wind and the relativistic electrons

In Figs. 3 and 4 the relativistic electron observations from the NOAA 12 spacecraft are displayed for January to March (Fig. 3) and from July to September (Fig. 4) in 1998. The figures also display solar wind density, speed and the IMF B_z from ACE and WIND spacecraft together with AE and Dst indices. Panels (e)–(g) show the relativistic electron flux measured by the NOAA 12 spacecraft in three different L regions. The red lines show the measurements for the evening sector and blue lines for the morning sector (colour on web version only). There is a tendency of higher flux of precipitating relativistic electrons in the evening sector compared to the morning sector. This gives an indication of a magnetic local time dependent process that scatters the relativistic electrons into the atmospheric loss cone. It is also worth pointing out the variation in the fluxes. As the spacecraft measures at different longitudes throughout the orbit, it also measures at different B-field strengths and thereby different particle fluxes. This gives the daily fluctuating nature in the relativistic electron fluxes.

Of interest in Fig. 3 is the CIR storm that begins at the end of day 69 and reaches a minimum Dst of −116 nT. Fig. 4 displays one CME storm that begins on day 218 which has minimum Dst of −138 nT, and one CME storm on day 239 with minimum Dst of −155 nT. Notice how the two CME storms show very different fluxes of relativistic electrons as displayed in panels (e)–(g) of Fig. 4 even though the strength of the storms is somewhat similar. This clearly shows how the intensity of the magnetic storm as measured by the Dst index does not determine the amount of relativistic electron losses to the atmosphere. During these storms the solar wind velocity is, however, very different and it has been shown by e.g. Baker et al. (1997) that this is a crucial parameter for the acceleration of electrons to relativistic energies. The CIR storm in Fig. 3 and the two CME storms in Fig. 4 are investigated in detail later in this paper. Table 4 provides a list of the three selected storms.

Table 4
List of the three selected CIR and CME storms

	Type	Day of year	Date
1	CIR, long 'recovery'	069–079, 1998	March 10–20, 1998
2	CME, short recovery	217–227, 1998	August 05–15, 1998
3	CME, long 'recovery'	237–247, 1998	August 25–September 04, 1998

4. Investigation of three storms

Figs. 5–7 show particle data from NOAA 12 and NOAA 14 (e)–(j) together with the solar wind density (a), IMF B_z, solar wind velocity (c), the AE index (d) and the Dst (k) from the three storms in Table 4. The observations are from the Northern Hemisphere and data from both the evening (17 MLT), the night (03 MLT), the morning (07 MLT) and the day (14 MLT) are presented (see Fig. 1 for the two spacecraft's MLT coverage).

The data are in hourly resolution except the IMF B_z component, which is in 16 s resolution to see the Alfvén waves better. The data in panels (e)–(j) are plotted on a logarithmic color scale versus L and time. Panel (e) exhibits 30–80 keV protons with 0° pitch angle, which is precipitating into the atmosphere. Panel (f) exhibits electrons >30 keV with 90° pitch angle, which is at the edge of the atmospheric loss cone. These electrons can be considered as 'seed' population for a local chorus-driven electron acceleration mechanism according to Meredith et al. (2003a) and Baker et al. (1998a, b). Panels (g)–(j) exhibit electrons >1.0 MeV, that is relativistic electrons near and within the atmospheric loss cone, detected by the dome detector.

4.1. *Description of the CIR storm*

Fig. 5 displays the observations from day 69 to 79 (March 10–20) in 1998. A solar wind fast stream of about 600 km/s emanating from a solar coronal hole interacts with an upstream slow stream of about 300 km/s and forms a CIR storm on day 69 (Richardson et al., 2006). In panel (a) we observe how the solar wind density exhibits a peak before it decreases rapidly. At the same time the solar wind speed displayed in panel (c) increases to almost 600 km/s. These features are typical

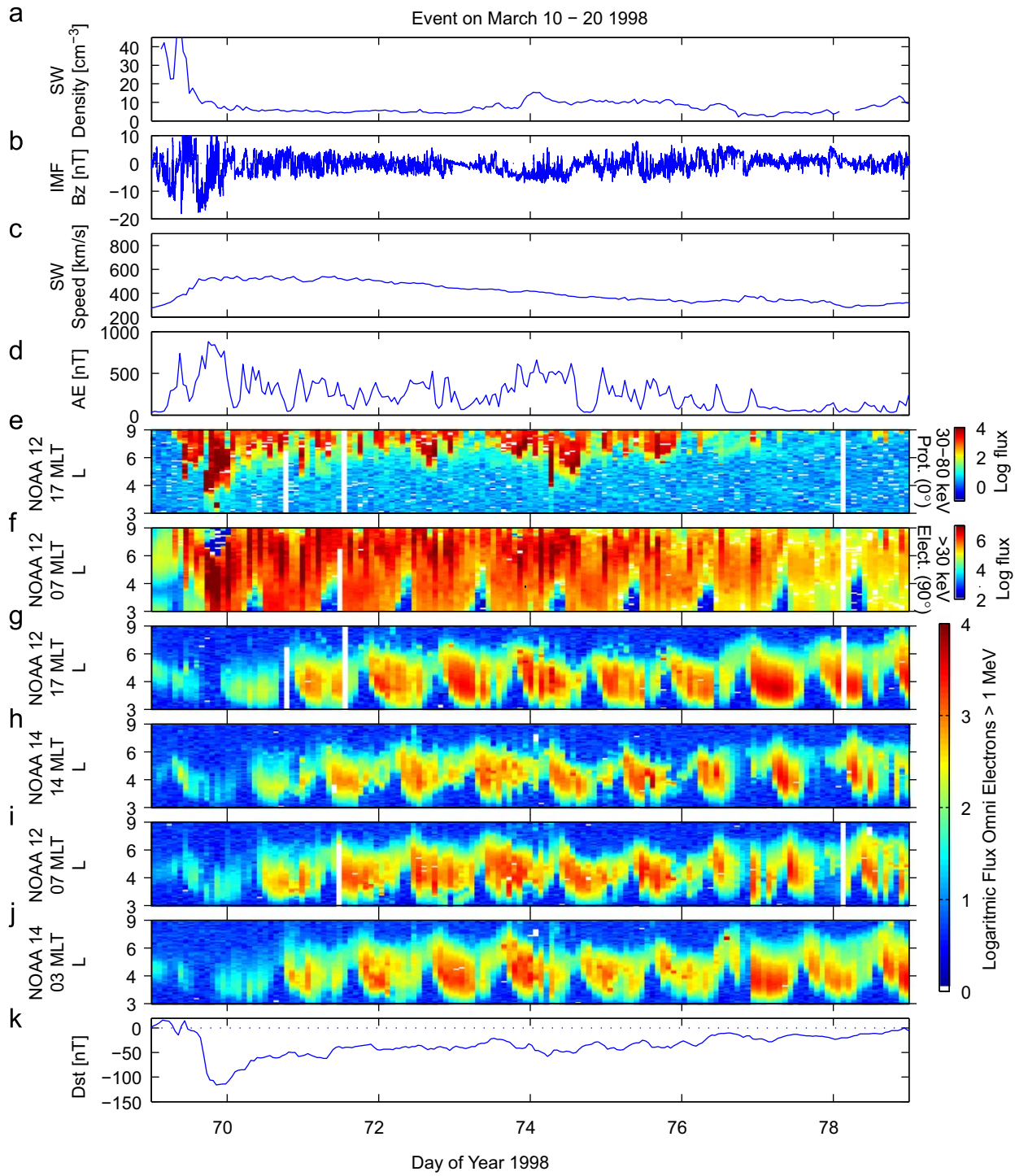

Fig. 5. The solar wind density, IMF B_z component (16 s resolution), solar wind velocity, AE and Dst indices for March 10–20, 1998, are displayed. Panels (e)–(j) display NOAA 12 and 14 data given in a format with a logarithmic color scale, plotted versus L and time. Panel (e) displays NOAA 12 protons (30–80 keV), while panel (f) shows electrons >30 keV. Panels (g)–(j) exhibit NOAA 12 and NOAA 14 energetic electrons >1.0 MeV sorted by magnetic time sectors 03, 07, 14 and 17 MLT. Panel (k) displays the Dst index.

for the CIR storms. The Dst reached −116 nT at the evening on day 69 and the storm exhibits a slow 'recovery'. The AE index reached as high as 881 nT during the main phase and continued to be elevated during the slow 'recovery' phase showing clear HILDCAA activity. This CIR storm has also been investigated by Richardson et al. (2006), Kataoka and Miyoshi (2006) and Gonzalez et al. (2007). The HILDCAA aspect of this storm has

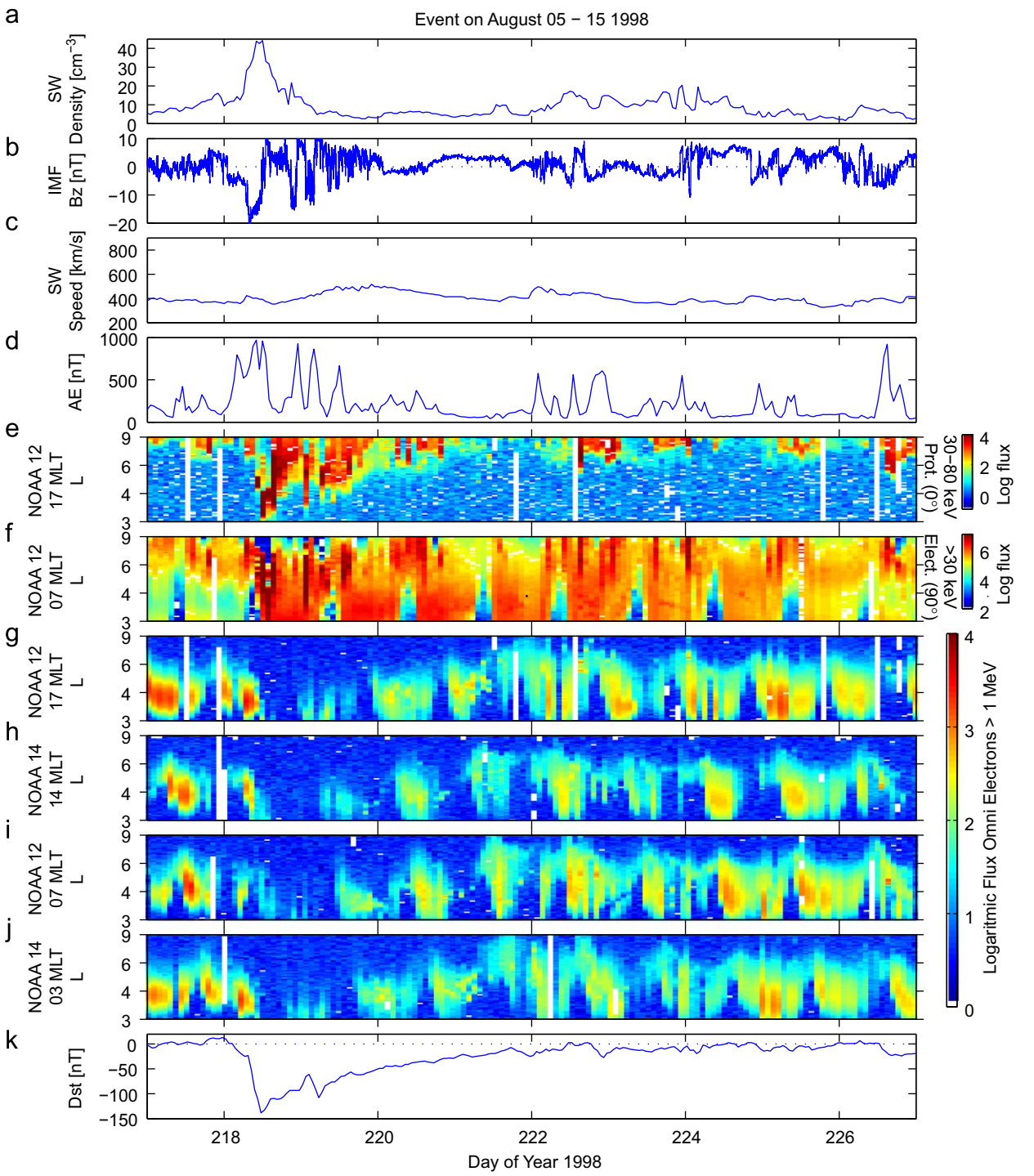

Fig. 6. The solar wind density, IMF B_z component (16 s resolution), solar wind velocity, AE and Dst indices for August 5–15, 1998, are displayed. Panels (e)–(j) display NOAA 12 and 14 data given in a format with a logarithmic color scale, plotted versus L and time. Panel (e) displays NOAA 12 protons (30–80 keV), while panel (f) shows electrons >30 keV. Panels (g)–(j) exhibit NOAA 12 and NOAA 14 energetic electrons >1.0 MeV sorted by magnetic time sectors 03, 07, 14 and 17 MLT. Panel (k) displays the Dst index.

been treated by Tsurutani et al. (2004). It is the long period of $B_z<0$ on day 69 that allows this storm to develop into a major geomagnetic storm. This is in accordance with Gonzalez and Tsurutani (1987) who concluded that $B_z>10$ nT for >3 h is necessary for a Dst <-10 nT storm to build up.

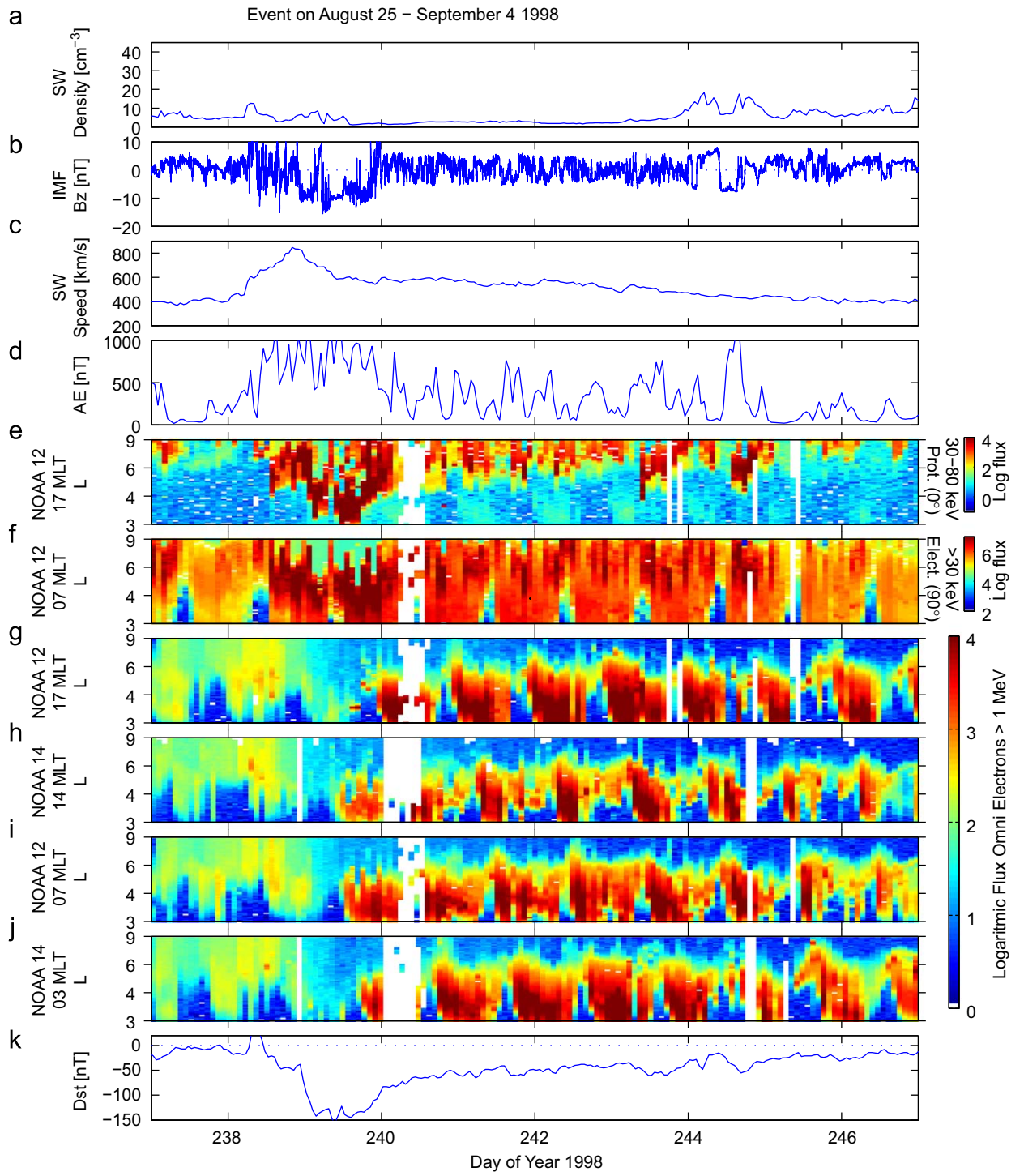

Fig. 7. The solar wind density, B_z component of IMF (16 s resolution), solar wind velocity, AE and Dst indices for August 25–September 4, 1998, are displayed. Panels (e)–(j) display NOAA 12 and 14 data given in a format with a logarithmic color scale, plotted versus L and time. Panel (e) displays NOAA 12 protons (30–80 keV), while panel (f) shows electrons >30 keV. Panels (g)–(j) exhibit NOAA 12 and NOAA 14 energetic electrons >1.0 MeV sorted by magnetic time sectors 03, 07, 14 and 17 MLT. Panel (k) displays the Dst index.

4.2. Description of the CME storm with long recovery phase

Fig. 6 displays the observations from day 217 to 227 (August 5–15) in 1998. The solar wind density (panel (a)) exhibits a peak in the beginning of the storm, but with a slightly slower decrease compared to the CIR storm in Fig. 5. The density increase was due to a CME on the Sun (Cane and Richardson, 2003). The solar wind speed

(panel (c)) increased more slowly compared to the CIR storm in Fig. 5. The Dst reached −138 nT on day 218 but recovered to quiet day values already at day 222. The AE index was elevated mainly during the main phase of the storm reaching as high as 970 nT, and the recovery phase exhibited no HILDCAA activity. The solar wind speed reached 530 km/s.

4.3. Description of the CME storm with fast recovery phase

Fig. 7 displays the observations from day 237 to 247 (August 25–September 4) in 1998. According to Cane and Richardson (2003) this storm is a CME storm. The Dst reached −155 nT at day 239 and during the main phase of the storm, AE reached 1300 nT. The following recovery phase exhibits a Dst that takes 8 days to recover to quiet day values. The AE index was elevated during the 5 first days of the recovery phase, having an average value of 339 nT and reaching as high as 1126 nT. The recovery phase exhibits HILDCAA activity. The fluctuation in IMF B_z and the high solar wind speed that is typical during HILDCAA events are seen in panels (b) and (c) of Fig. 7. Just before day 239, the solar wind speed reaches as high as 850 km/s.

5. The proton injection during storms

The proton injections into the ring current displayed in Figs. 5(e), 6(e) and 7(e) show how protons penetrate deep into the ring current during the main phase of the storms. During the recovery phase of the storm displayed in Fig. 6(e), there are more or less no additional protons injected. While there are no 'fresh' protons injected into the ring current to balance the recovery of the Dst index, there will not be a prolonged recovery phase either. In Figs. 5(e) and 7(e) the recovery phase with HILDCAA is associated with particle injection into the outer part of the ring current. The injected protons penetrate deep enough into the ring current to have an influence on the Dst index, but their energy content and depth of penetration is not large enough to cause a new magnetic storm (Sandanger et al., 2005).

Figs. 5(g)–(j) reveal very low intensities of relativistic electrons before the geomagnetic storm begins, while Figs. 6(g)–(j) reveal some higher intensities. Figs. 7(g)–(j) show that the dome detector measure medium to low intensities at high L-values before the initial phase of the magnetic storm. This is due to a solar proton event. This solar proton event at the end of August was mentioned earlier and also displayed in Fig. 2.

During the main phase of the three storms the relativistic electrons are not present. This implies that there are no relativistic electrons in and near the atmospheric loss cone. But throughout the recovery phase of the geomagnetic storms, the relativistic electrons appear with high intensities in Figs. 5(g)–(j) and 7(g)–(j), while in Figs. 6(g)–(j) the intensity does not recover to pre-storm levels.

The relativistic electron precipitation is spatially structured both in time and L, indicating a scattering mechanism, that scatters the relativistic electrons into the atmospheric loss cone that is similarly structured.

5.1. Individual passes

Fig. 8 shows a morning pole-to-pole pass by NOAA 12 on August 10, 1998. During the pass the NOAA 12

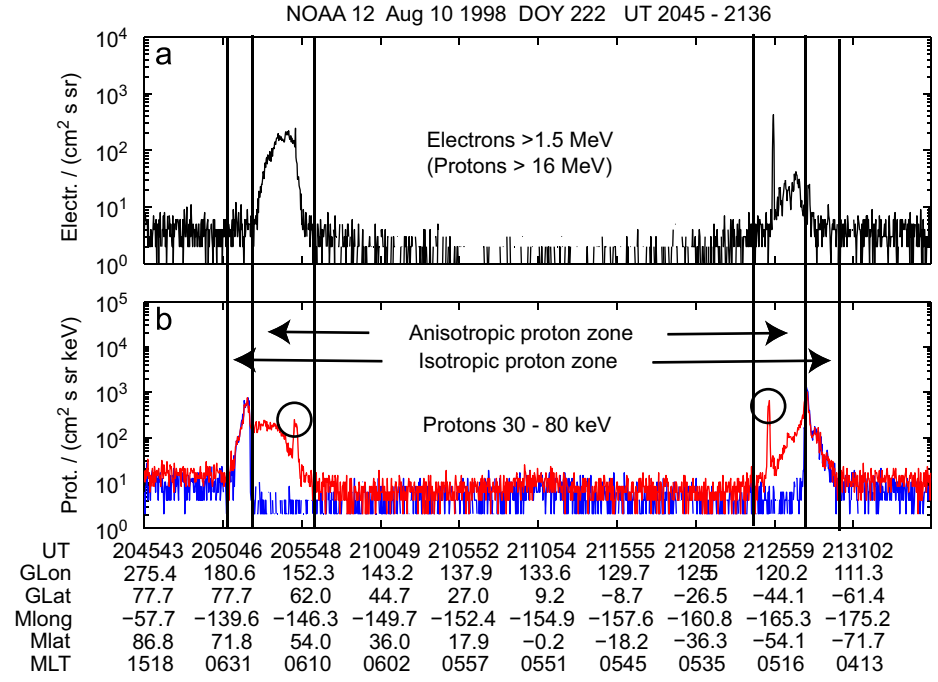

Fig. 8. Data taken during a pole-to-pole pass by NOAA 12 on August 10, 1998. Panel (a) exhibits flux of >1.0 MeV electrons, panel (b) exhibits flux of 30–80 keV protons measured by the vertical detector (blue dashed line) and the horizontal detector (red solid line). For colour, please see the web.

spacecraft observes first the isotropic proton zone between 2051 and 2052 UT. Immediately equatorward of this is the anisotropic proton zone. As the spacecraft crosses the equator and gets to the other hemisphere, it again encounters the anisotropic zone and then the isotropic zone. The boundary between the anisotropic zone and the isotropic zone is called the isotropic boundary. Sergeev et al. (1983) found the isotropic flux to be caused by pitch angle scattering in the equatorial current sheet. Here the magnetic field is so stretched that the first adiabatic invariant is violated and particles are effectively scattered into the loss cone giving rise to an

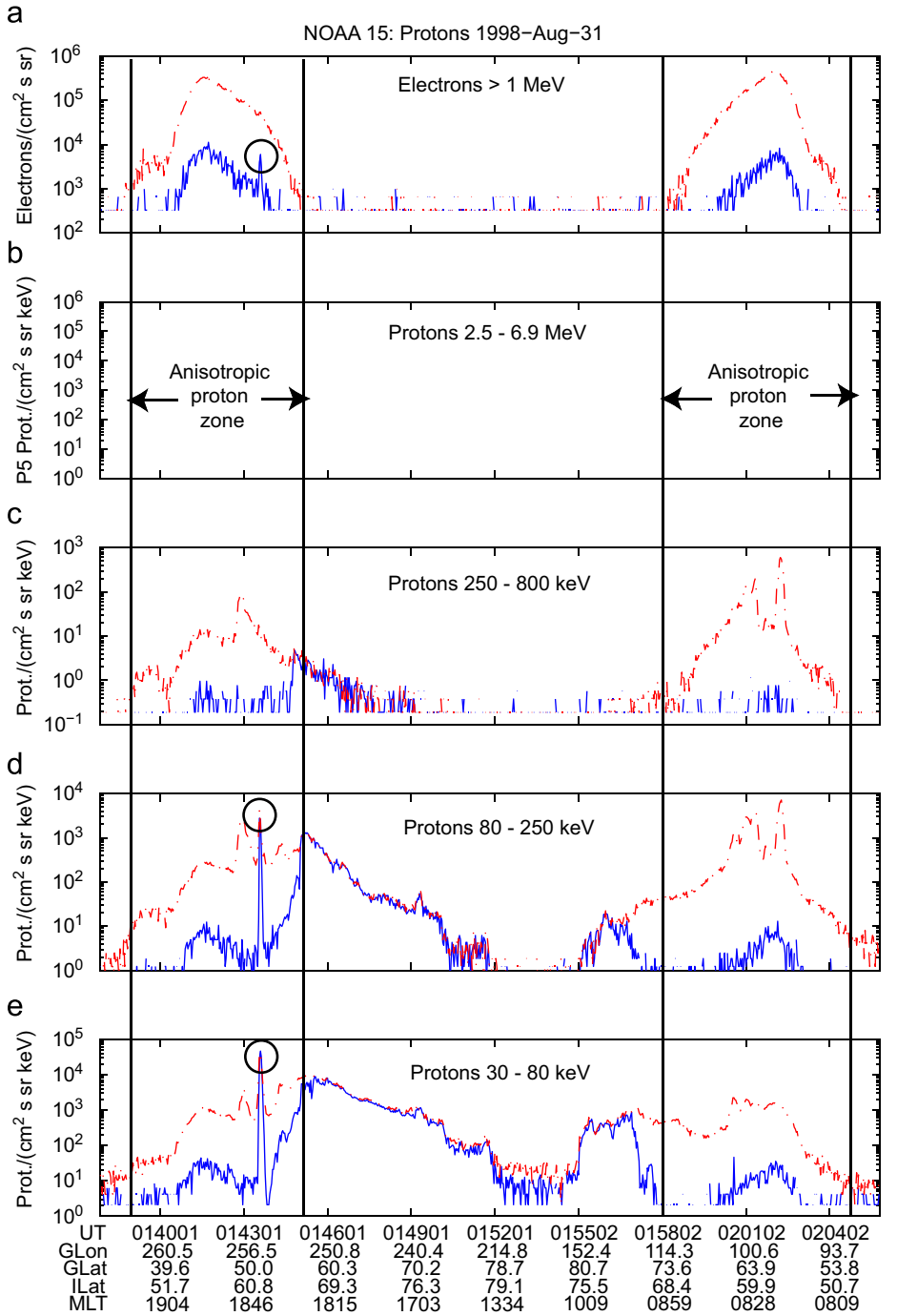

Fig. 9. Data taken during a low latitude-pole-low latitude pass by NOAA 15 on August 31, 1998. The five panels exhibit from the top: (a) flux of >1 MeV electrons (channel intended to measure >6.9 MeV protons), (b) flux of 2.5–6.9 MeV protons, (c) flux of 250–800 keV protons, (d) flux of 80–250 keV protons and finally, (e) flux of 30–80 keV protons. All fluxes measured by the vertical detector are marked as blue dashed line and all fluxes measured by the horizontal detector are marked by the red solid line. For colour, please see the web.

isotropic precipitation. Closer to the Earth the magnetic field lines are more dipolar, and the particle motion is more adiabatic, and the protons are not subjected to chaotic scattering into the loss cone. Here the trapped population prevails and the zone is called the anisotropic proton zone. In the isotropic proton zone, the protons are stable to EMIC wave growth, while in the anisotropic proton zone the protons are unstable to EMIC wave growth.

Fig. 9 shows a evening to morning pass by NOAA 15 from low latitude-pole-low latitude on August 15, 1998. The spacecraft observes the eveningside anisotropic zone and the isotropic proton zone immediately poleward. As the spacecraft crosses the polar cap and gets to the morningside the spacecraft observes the isotropic proton zone and the anisotropic proton zone immediately equatorward. The SEM-2 P6 proton telescope can monitor >1 MeV electrons as well as the >6.9 MeV protons it was intended to measure. In Fig. 9 we can use the P5 channel that measures 2.5–6.9 MeV protons to decide whether high energy protons are present or not. Fig. 9(b) shows that no 2.5–6.9 MeV protons (P5) are present at the same time as the P6 proton telescope in panel (a) shows high fluxes. This would be an unphysical proton energy distribution and we conclude that the flux measured in Fig. 9(a) is in fact >1 MeV electrons.

6. Intense spatially confined loss of ring current ions

In our data set we find all of the proton precipitation spikes inside the anisotropic proton zone, where the protons are unstable to EMIC wave growth. (The anisotropic proton zone is visualized in Figs. 8 and 9.) Regions of high

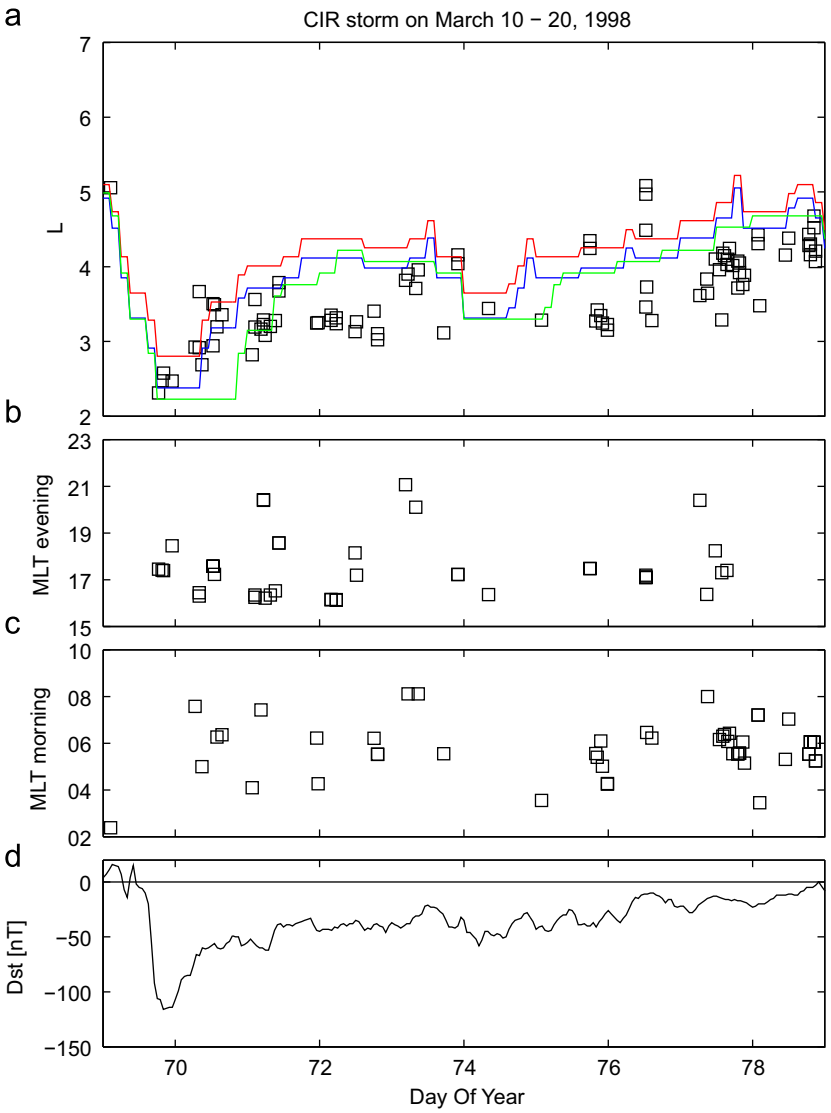

Fig. 10. Data from March 10–20, 1998. A total of 30–80 keV proton flux spikes found in the NOAA 12 (squares) data set are displayed as L versus time in panel (a). The maximum and minimum Kp based plasmapause location model by Moldwin et al. (2002) are displayed in red and blue, and the model by Carpenter and Anderson (1992) is displayed in green. In panels (b) and (c) the intensity spikes are plotted as MLT versus time for, respectively, the evening and morning sectors. The Dst index is displayed in panel (d). For colour, please see the web.

plasma density and/or weak magnetic field are favorable locations for strong EMIC wave–particle interactions. Such localized areas will give precipitation spikes like those presented in Figs. 8 and 9. Fig. 9 clearly shows that the pitch angle scattering of protons is so strong that we have isotropic proton precipitation inside the anisotropic proton zone; in a localized region the loss cone is completely filled in the two lowest proton energy channels (marked with a circle in panels (d) and (e)). The relativistic electrons displayed in panel (a) also exhibit a precipitation spike in the same localized region (also marked with a circle). We have also observed a localized burst of only trapped protons inside the anisotropic proton zone. In this section we will investigate localized bursts of precipitating and locally trapped 30–80 keV protons within the anisotropic proton zone for our three selected storms.

Interesting questions to ask are: Will there be different numbers of proton precipitation spikes for the three types of storms? Will the amount of proton precipitation spikes change throughout the different storm phases? What is the L and MLT dependence for the proton precipitation spikes? In order to answer these questions, localized precipitation spikes like those marked with a circle in Figs. 8 (NOAA 12) and 9 (NOAA 15) are picked out from all available NOAA passes during the three storms. NOAA 14 had some problems with the 30–80 keV 0° proton telescope that made it difficult to determine localized

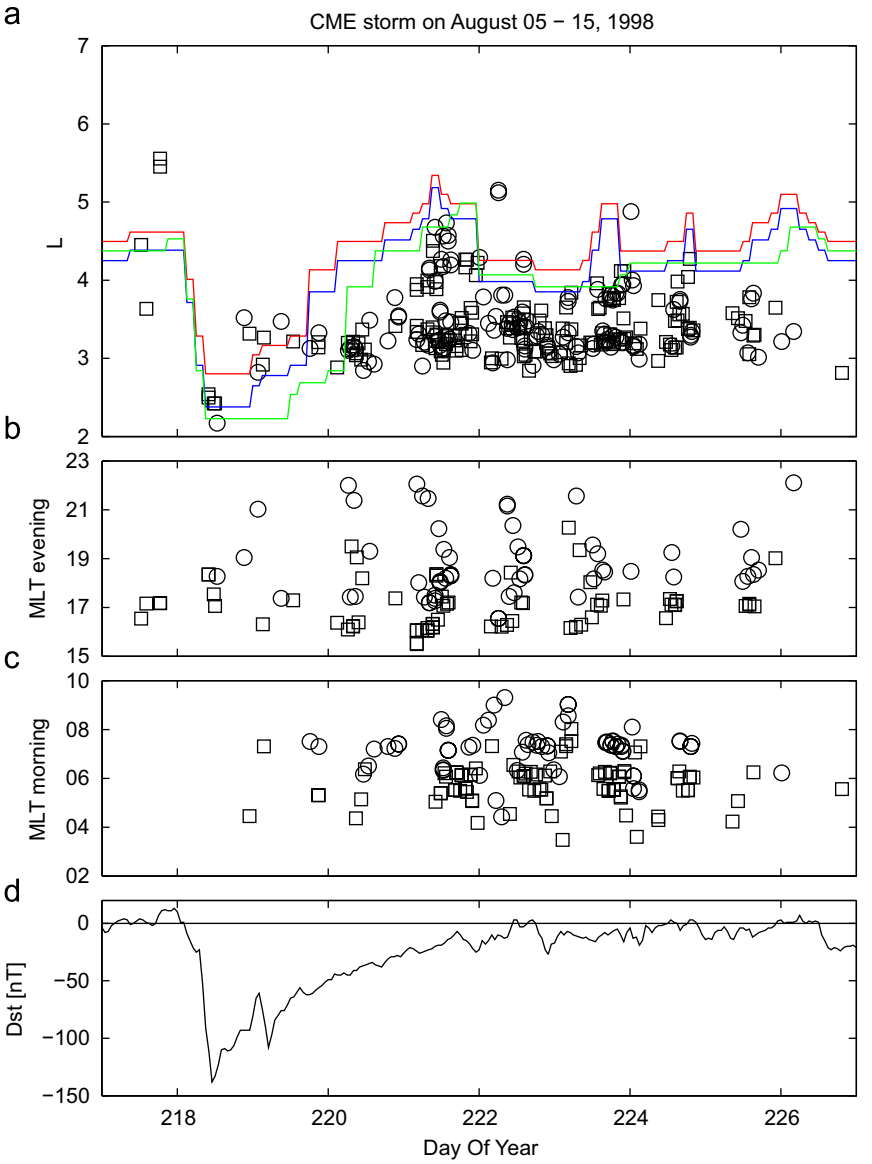

Fig. 11. Data from August 5 to 15, 1998. A total of 30–80 keV proton flux spikes found in the NOAA 12 (squares) and NOAA 15 (circles) data set are displayed as L versus time in panel (a). The maximum and minimum Kp based plasmapause location model by Moldwin et al. (2002) are displayed in red and blue, and the model by Carpenter and Anderson (1992) is displayed in green. In panels (b) and (c) the intensity spikes are plotted as MLT versus time for, respectively, the evening and morning sectors. The Dst index is displayed in panel (d). For colour, please see the web.

proton precipitation spikes and is therefore not used. The first storm on day 69–79 will only be covered by NOAA 12, because NOAA 15 was not launched at that time. The second and third storm will be covered by both NOAA 12 and NOAA 15.

In Figs. 10–12 the NOAA 12 precipitation spikes are marked with a square, while NOAA 15 precipitation spikes are marked with a circle. The detected precipitation spikes are plotted as L versus time in panel (a) and as MLT versus time in panels (b) and (c). The Dst index is displayed in panel (d). In panel (a) of Figs. 10–12 we have included the statistical position of the plasmapause. The red and blue lines correspond to the maximum and minimum plasmapause location according to the model provided by Moldwin et al. (2002) (colour on web version only). The green line corresponds to the plasmapause location according to Carpenter and Anderson (1992) (colour on web version only). In panels (b) and (c) the spikes show a pattern in MLT versus time. This is because the spacecraft measure at different MLTs from pass to pass.

We will compare the CIR storm (Fig. 10) with slow 'recovery' phase (HILDCAA) with the two CME storms. The first CME storm in Fig. 11 shows a fast recovery phase (no-HILDCAA) while the second CME storm (Fig. 12) shows a slow 'recovery' phase (HILDCAA). It is difficult to tell whether the different storms produce different amount of proton precipitation spikes since the spacecraft coverage vary for the three storms. But the CME storm with fast

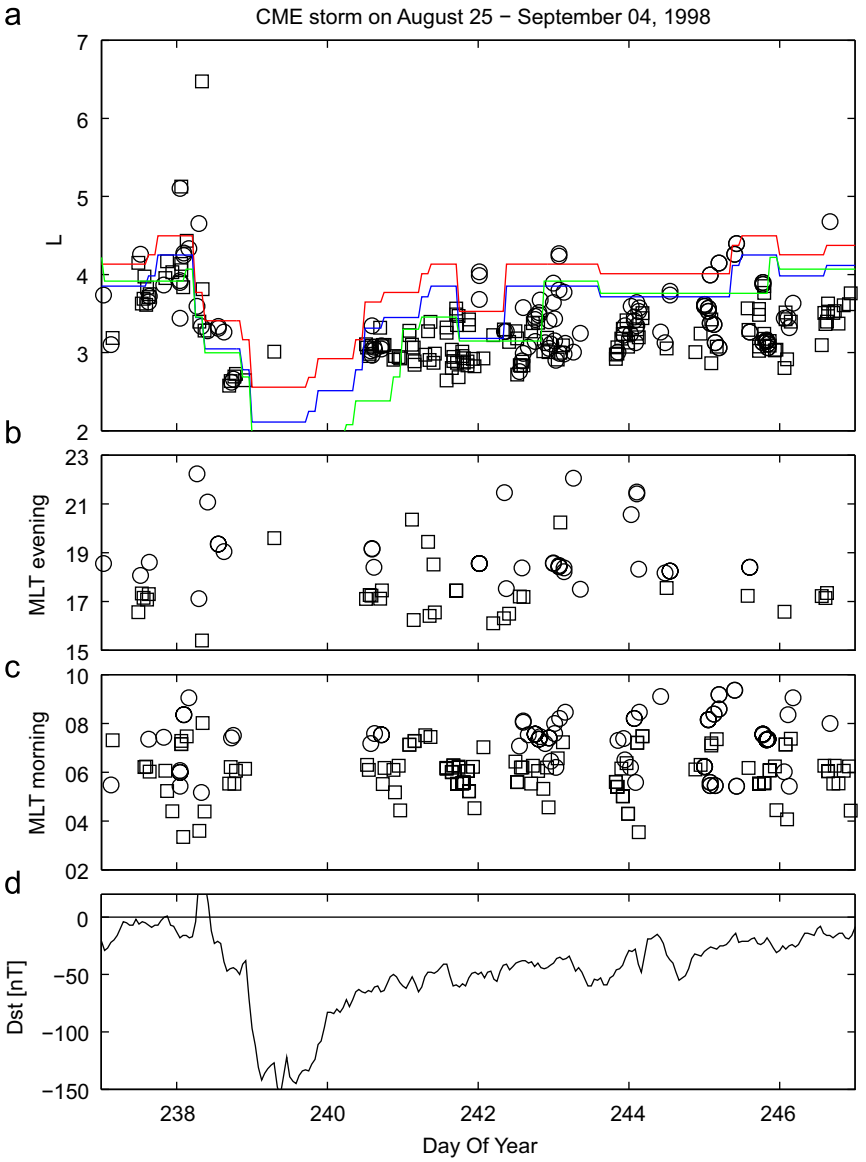

Fig. 12. Data from August 25 to September 4, 1998. A total of 30–80 keV proton flux spikes found in the NOAA 12 (squares) and NOAA 15 (circles) data set are displayed as L versus time in panel (a). The maximum and minimum Kp based plasmapause location model by Moldwin et al. (2002) are displayed in red and blue, and the model by Carpenter and Anderson (1992) is displayed in green. In panels (b) and (c) the intensity spikes are plotted as MLT versus time for, respectively, the evening and morning sectors. The Dst index is displayed in panel (d). For colour, please see the web.

recovery (Fig. 11) and the CME storm with slow 'recovery' phase (Fig. 12) have the same spacecraft coverage throughout the 10 days displayed, and the spacecraft detect around 150 proton precipitation spikes per spacecraft for each of the two storms. The CIR storm with slow 'recovery' phase has only NOAA 12 coverage and the spacecraft detects around 100 proton precipitation spikes throughout the 10 days displayed. This might indicate that the CIR storm in Fig. 10 produce less proton precipitation spikes than the two CME storms in Figs. 11 and 12.

The number of proton precipitation spikes seems to change throughout the different storm phases. There are fewer proton precipitation spikes in the main phase than in the recovery phase. This is clearer for the two CME storms than for the CIR storm. The difference between the CME and CIR storm might be due to fewer spikes in the CIR storm.

Fig. 13 displays all observed proton precipitation spikes (both from the Northern and Southern Hemispheres) during the 10 days period for all three storms as a function of L and MLT. The red and blue lines correspond to the maximum and minimum plasmapause location throughout the storm according to the Kp based model provided by Moldwin et al. (2002) (colour on web version only). Most of the proton precipitation spikes shown in Fig. 13 are located inside the calculated plasmapause, and only a few are located on the outside. If we compare the L position of the spike and the calculated plasmapause location at the same UT, we find that 88% of the spikes in the CIR storm are located inside the maximum plasmapause location (the red curve in Fig. 10). In the first CME storm 96% of the spikes are inside the calculated plasmapause and in the second CME storm 93% are inside.

6.1. *The spike locations compared with simultaneous IMAGE observations of the plasmapause*

In order to compare the location of the proton precipitation spikes with simultaneous observations of the plasmapause location we have to move from year 1998 to 2001 when we have IMAGE data of the plasmasphere. The plasmapause location found by Spasojević et al. (2003) using the IMAGE data and the 30–80 keV proton flux spikes detected by NOAA 15 and NOAA 16 are displayed together in Fig. 14. The two different plasmapause locations seen in the figure are from 1705 and 2121 UT. We can see how the spikes are located inside and close to the plasmapause.

7. Discussions and conclusions

Our main objective in this study was to relate the loss of relativistic electrons to low altitude observations of ring current protons during CIR and CME storms. Three storms were selected, one CIR and two CME storms, one of these with a slow 'recovery' phase and one with a fast recovery phase. The CIR and the CME with a long 'recovery' phase were both connected to high-speed streams known to

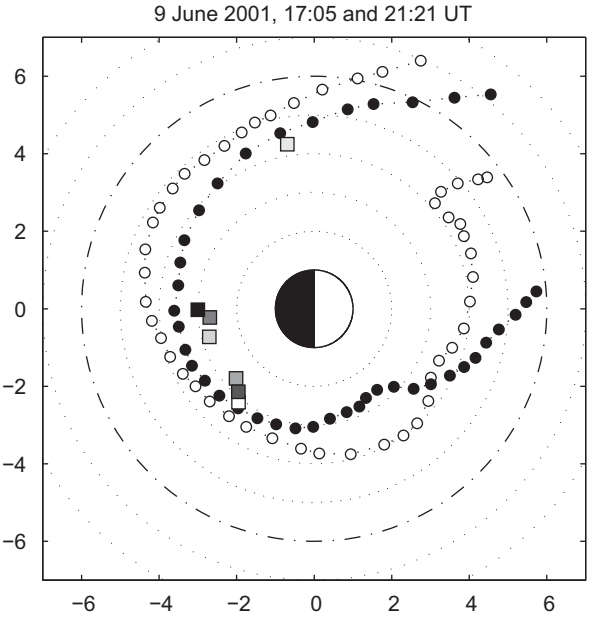

Fig. 14. Data from June 9, 2001. The plasmapause location at 1705 UT (white circles) and 2121 UT (black circles) found by Spasojević et al. (2003) using the IMAGE data are plotted together with 30–80 keV proton flux spikes (squares) found in the NOAA 15 and NOAA 16 data set. The white squares are proton flux spikes observed close to 1705 UT, while the black squares are spikes observed close to 2121 UT.

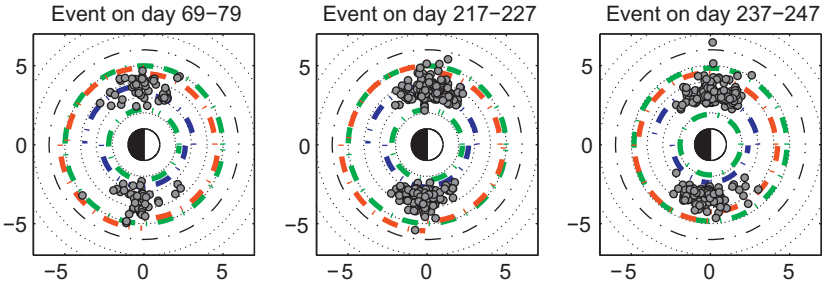

Fig. 13. The proton precipitation spikes observed throughout the 10 days are plotted as function of L and MLT for all three storms investigated. The maximum and minimum Kp based plasmapause location model by Moldwin et al. (2002) are displayed in red and blue, and the model by Carpenter and Anderson (1992) is displayed in green. The MLT distribution of the proton precipitation spikes show the coverage of the NOAA 12 and NOAA 15 spacecraft (see Fig. 1). For colour, please see the web.

accelerate electrons up to relativistic energies throughout the 'recovery' phase.

7.1. The loss of relativistic electrons

We investigate loss of relativistic electrons due to pitch angle scattering from wave–particle interactions. Possible waves that can resonate with electrons and be responsible for pitch angle scattering and losses are plasmaspheric hiss, whistler mode chorus and EMIC waves. EMIC waves may produce rapid scattering of relativistic electrons near the edge of the loss cone (Meredith et al., 2003b), while whistler mode chorus waves maximize for particles with equatorial pitch angles above 30° (Horne et al., 2005). According to Shprits et al. (2006), hiss and chorus scatter relativistic electrons at higher pitch angles, while EMIC waves are very effective in scattering near the loss cone, thereby controlling the loss rate of relativistic electrons.

We conclude that EMIC waves are responsible for the relativistic electron losses observed in the anisotropic proton zone. This loss mechanism seem to be present during all three storms. The proton energy density in the ring current for the three storms considered was approximately the same judging from their Dst values. The CIR storm had a Dst −100 nT, the CME storm −135 nT and the CME storm with long 'recovery' −150 nT. As a first approximation we can assume that the production of EMIC waves is about equal during the storms. The production of EMIC waves will also depend on the density of cold plasma location, etc.

It is known that there is higher flux of relativistic electrons in the radiation belt during storms with long 'recovery' phases. That is, in the storms with high solar wind speed and Alfvén waves in the IMF B_z we should observe higher losses of relativistic electrons inside the anisotropic proton zone if the source, the radiation belt, determines the loss. This is what we observed in Figs. 5–7 panels (g)–(j). The storms with long 'recovery' phase give the highest loss. The amount of relativistic electrons that will be lost is decided by the amount of electrons that have been accelerated, that is their intensity in the radiation belt. In order to substantiate this statement the measured loss rate will be compared with the intensity in the radiation belt. For the three storms an approximate loss of relativistic electrons with energies >1 MeV to the atmosphere is displayed in Table 5.

In order to get an estimate of the flux of relativistic electrons in the radiation belt, measurements by the LANL satellites near the Earths equator at $L = 6.6$ are used (Geoff Reeves, private communication). These measurements of electrons in the energy range (0.8–1.8 MeV) are displayed in Table 5 and show clearly that the CME storm with long 'recovery' has the highest intensity, than the CIR storm, and the CME storm with the fast recovery phase has the lowest intensity.

This relation between the storm relativistic electron intensities in the radiation belt is thus the same as the loss to the atmosphere observed by the NOAA spacecraft. We can thus conclude that during the storms considered it is the intensity of relativistic electrons in the radiation belt which is the limiting factor for their loss to the atmosphere.

7.2. Spatial distribution of the loss

The relativistic electron precipitation displayed in Figs. 3 and 4 shows higher intensities in the evening sector than in the morning sector, while the relativistic electron precipitation displayed in Figs. 5–7 is spatially structured both in time and L. This indicates a scattering mechanism that is spatially structured both in time and L, and magnetic local time dependent. It is important to notice that even though the scattering mechanism seems to have a MLT dependence, we observe loss of relativistic electrons throughout all MLT sectors.

According to Erlandson and Ukhorskiy (2001) EMIC waves are preferentially excited along the duskside of the plasmasphere and in the regions of plumes, where ring current ions interact with high-density plasma. Sandanger et al. (2007) and the present study observe loss of relativistic electrons at all MLT sectors and conclude that EMIC waves can resonate and scatter relativistic electrons throughout all MLT sectors, not only at the duskside.

In the single passes displayed in Figs. 8 and 9 we observe how the loss of relativistic electrons is inside the anisotropic proton zone. This agrees with Sandanger et al. (2007) that showed that the losses are due to weak pitch angle scattering due to EMIC wave growth inside the whole unstable anisotropic proton zone. Localized losses of ring current ions, also called proton precipitation spikes, seem to be equally present during the CME storm with slow 'recovery' phase than during the CME storm with fast recovery phase. The CIR storm with slow 'recovery' phase had only half of the spacecraft coverage and only one-third of the proton precipitation spikes compared to the two CME storms. This might indicate some differences, but it is not enough to be conclusive. We observe fewer proton precipitation spikes in the main phase of the three storms than in the recovery phases of the storms. The proton precipitation spikes are observed

Table 5
The table list the three selected CIR and CME storms and their loss of >1 MeV electrons to the atmosphere and flux of 0.8–1.8 MeV electrons in the radiation belt (Geoff Reeves, private communication)

	Type of storm	Loss to the atmosphere	Flux in the radiation belt
1	CIR, long 'recovery'	4×10^4 electrons/cm^2 s sr	100 electrons/cm^2 s sr keV
2	CME, short recovery	10^4 electrons/cm^2 s sr	50 electrons/cm^2 s sr keV
3	CME, long 'recovery'	10^5 electrons/cm^2 s sr	130 electrons/cm^2 s sr keV

at all MLT sectors, but there seem to be slightly more proton precipitation spikes in the morning MLT sector than in the evening MLT sector.

7.3. Loss related to the plasmapause

When using a Kp based plasmapause location model and IMAGE data we conclude that the proton precipitation spikes are located inside the plasmapause. This is also supported by numerous earlier works. The proton precipitation spikes are due to medium to strong pitch angle diffusion due to wave–particle interaction at favorable locations for strong EMIC wave growth. The proton precipitation spikes are visualized as proton aurora spots on the ground and are particle counterparts of Pc1 pulsations (Søraas et al., 1999; Yahnina et al., 2000, 2002, 2003; Yahnin et al., 2007). Yahnin et al. (2007) suggest the source of the Pc1 pulsation, EMIC waves and strong scattering of protons into the loss cone (the proton precipitation spikes), to be associated with an azimuthal gradient of cold plasma that appears due to a ripple at the plasmapause.

Future work in this area could be to combine relativistic electron data from the polar orbiting NOAA spacecraft with data from geosynchronous spacecraft. In that way particle fluxes with small pitch angles can be compared in detail with particle fluxes with large pitch angles.

Acknowledgments

The authors thank the Norwegian Research Council for financial support to the Space Research program. Furthermore, we thank Maria Spasojević for providing plasmapause data and Geoff Reeves for providing LANL data (http://leadbelly.lanl.gov/). We thank the ACE spacecraft team, the WIND spacecraft team, CDA Web and the Space Physics Data Facility (SPDF) and National Space Science Data Center (NSSDC) for providing solar wind parameters. We also acknowledge World Data Center for Geomagnetism, Kyoto, for providing magnetic activity indices. Coronal hole information was extracted from the Space Weather Prediction Center, Boulder, CO, National Oceanic and Atmospheric Administration (NOAA), US Department of Commerce (http://www.swpc.noaa.gov/).

References

Baker, D.N., Li, X., Turner, N., Allen, J.H., Bargatze, L.F., Blake, J.B., Sheldon, R.B., Spence, H.E., Belian, R.D., Reeves, G.D., Kanekal, S.G., Klecker, B., Lepping, R.P., Ogilvie, K., Mewaldt, R.A., Onsager, T., Singer, H.J., Rostoker, G., 1997. Recurrent geomagnetic storms and relativistic electron enhancements in the outer magnetosphere: ISTP coordinated measurements. Journal of Geophysical Research 102 (A7), 14141.

Baker, D.N., Pulkkinen, T., Li, X., Kanekal, S., Blake, B., Selesnick, R., Henderson, E., Reeves, G., Spence, H., Rostoker, G., 1998a. Coronal mass ejections, magnetic clouds, and relativistic magnetospheric electron events: ISTP. Journal of Geophysical Research 103, 17279.

Baker, D.N., Pulkkinen, T.I., Li, X., Kanekal, S., Ogilvie, K.W., Lepping, R.P., Blake, J.B., Callis, L.B., Rostoker, G., Singer, H.J., Reeves, G.D., 1998b. A strong CME-related magnetic cloud interaction with the earth's magnetosphere: ISTP observations of rapid relativistic electron acceleration on May 15. Geophysical Research Letters 25 (15), 2975.

Borovsky, J.E., Denton, M.H., 2006. Differences between CME-driven storms and CIR-driven storms. Journal of Geophysical Research 111 (A07S08).

Cane, H.V., Richardson, I.G., 2003. Interplanetary coronal mass ejections in the near-earth solar wind during 1996–2002. Journal of Geophysical Research 108 (A4).

Carpenter, D.L., Anderson, R.R., 1992. An ISEE/whistler model of equatorial electron density in the magnetosphere. Journal of Geophysical Research 97, 1097.

Cornwall, J.M., Coroniti, F.V., Thorne, R.M., 1971. Unified theory of SAR arc formation at the plasmapause. Journal of Geophysical Research 76 (19), 4428.

Erlandson, R.E., Ukhorskiy, A.J., 2001. Observations of electromagnetic ion cyclotron waves during geomagnetic storms: wave occurrence and pitch angle scattering. Journal of Geophysical Research 106 (A3), 3883.

Evans, D.S., Greer, M.S., 2000. Polar orbiting environmental satellite space environment monitor 2: instrument description and archive data documentation. NOAA Technical Memorandum, June.

Friedel, R.H.W., Reeves, G.D., Obara, T., 2002. Relativistic electron dynamics in the inner magnetosphere—a review. Journal of Atmospheric and Solar-Terrestrial Physics 64, 265.

Gonzalez, W.D., Tsurutani, B.T., 1987. Criteria of interplanetary parameters causing intense magnetic storms ($Dst < -100$ nT). Planetary and Space Science 35, 1101.

Gonzalez, W.D., Echer, E., Clua-Gonzalez, A.L., Tsurutani, B.T., 2007. Interplanetary origin of intense geomagnetic storms ($Dst < -100$ nT) during solar cycle 23. Geophysical Research Letters 34 (L06101).

Guarnieri, F.L., Tsurutani, B.T., Gonzalez, W.D., Echer, E., Clua-Gonzalez, A.L., Grande, M., Søraas, F., 2006. ICME and CIR storms with particular emphasis on HILDCAA events. In: ILWS Workshop 2006, GOA, February 19–20.

Horne, R.B., Thorne, R.M., 1998. Potential waves for relativistic electron scattering and stochastic acceleration during magnetic storms. Geophysical Research Letters 25 (15), 3011.

Horne, R.B., Thorne, R.M., Glauert, S.A., Albert, J.M., Meredith, N.P., Anderson, R.R., 2005. Timescales for radiation belt electron acceleration by whistler mode chorus. Journal of Geophysical Research 110 (A03225).

Kataoka, R., Miyoshi, Y., 2006. Flux enhancement of radiation belt electrons during geomagnetic storms driven by coronal mass ejections and corotating interaction regions. Space Weather 4 (S09004).

Lundblad, J.A., Søraas, F., 1978. Proton observations supporting the ion cyclotron wave theory of SAR arc formation. Planetary and Space Science 26 (3), 245.

Mann, I.R., O'Brian, T.P., Milling, D.K., 2004. Correlations between ULF wave power, solar wind speed, and relativistic electron flux in the magnetosphere: solar cycle dependence. Journal of Atmospheric and Solar-Terrestrial Physics 66, 187.

Meredith, N.P., Cain, M., Horne, R.B., Thorne, R.M., Summers, D., Anderson, R.R., 2003a. Evidence for chorus-driven electron acceleration to relativistic energies from a survey of geomagnetically disturbed periods. Journal of Geophysical Research 108 (A6), 1248.

Meredith, N.P., Thorne, R.M., Horne, R.B., Summers, D., Fraser, B.J., Anderson, R.R., 2003b. Statistical analysis of relativistic electron energies for cyclotron resonance with EMIC waves observed on CRRES. Journal of Geophysical Research 108 (A6), 1250.

Miyoshi, Y., Kataoka, R., 2005. Ring current ions and radiation belt electrons during geomagnetic storms driven by coronal mass ejections and corotating interaction regions. Geophysical Research Letters 32 (L21105).

Miyoshi, Y., Jordanova, V.K., Morioka, A., Evans, D.S., 2004. Solar cycle variations of the electron radiation belts: observations and radial diffusion simulation. Space Weather 2 (S10S02).

Moldwin, M.B., Downward, L., Rassoul, H.K., Amin, R., Anderson, R.R., 2002. A new model of the location of the plasmapause: CRRES results. Journal of Geophysical Research 107 (A11), 1339.

O'Brien, T.P., McPherron, R.L., Sornette, D., Reeves, G.D., Friedel, R., Singer, H.J., 2001. Which magnetic storms produce relativistic electrons at geosynchronous orbit? Journal of Geophysical Research 106, 15533.

Raben, V.J., Evans, D.S., Sauer, H.H., Sahm, S.R., Huynh, M., 1995. TIROS/NOAA satellite space environment monitor data archive documentation: 1995 update. NOAA Technical Memorandum ERL SEL-86, February.

Reeves, G.D., McAdams, K.L., Friedel, R.H.W., O'Brien, T.P., 2003. Acceleration and loss of relativistic electrons during geomagnetic storms. Geophysical Research Letters 30 (10), 1529.

Richardson, I.G., Webb, D.F., Zhang, J., Berdichevsky, D.B., Biesecker, D.A., Kasper, J.C., Kataoka, R., Steinberg, J.T., Thompson, B.J., Wu, C.-C., Zhukov, A.N., 2006. Major geomagnetic storms ($Dst \leqslant -100$ nT) generated by corotating interaction regions. Journal of Geophysical Research 111 (A07S09).

Sandanger, M.I., Søraas, F., Aarsnes, K., Oksavik, K., Evans, D.S., Greer, M.S., 2005. Proton injections into the ring current associated with B_z variations during HILDCAA events. In: Pulkkinen, T.I., Tsyganenko, N.A., Friedel, R.H.W. (Eds.), The Inner Magnetosphere: Physics and Modeling. Geophysical Monograph Series, vol. 155. AGU, Washington, DC, p. 249.

Sandanger, M.I., Søraas, F., Aarsnes, K., Oksavik, K., Evans, D.S., 2007. Loss of relativistic electrons: evidence for pitch angle scattering by electromagnetic ion cyclotron waves excited by unstable ring current protons. Journal of Geophysical Research 112 (A12213).

Sergeev, V.A., Sazhina, E.M., Tsyganenko, N.A., Lundblad, J.A., Søraas, F., 1983. Pitch-angle scattering of energetic protons in the magnetotail current sheet as the dominant source of their isotropic precipitation into the nightside ionosphere. Planetary and Space Science 31 (10), 1147.

Shprits, Y.Y., Li, W., Thorne, R.M., 2006. Controlling effect of the pitch angle scattering rates near the edge of the loss cone on electron lifetimes. Journal of Geophysical Research 111 (A12206).

Søraas, F., Aarsnes, K., Lundblad, J.Å., Evans, D.S., 1999. Enhanced pitch angle scattering of protons at mid-latitudes during geomagnetic storms. Physics and Chemistry of the Earth (C) 24 (1–3), 287.

Søraas, F., Aarsnes, K., Oksavik, K., Sandanger, M.I., Evans, D.S., Greer, M.S., 2004. Evidence for particle injection as the cause of Dst reduction during HILDCAA events. Journal of Atmospheric and Solar-Terrestrial Physics 66 (2), 177.

Spasojević, M., Goldstein, J., Carpenter, D.L., Inan, U.S., Sandel, B.R., Moldwin, M.B., Reinisch, B.W., 2003. Global response of the plasmasphere to a geomagnetic disturbance. Journal of Geophysical Research 108 (A9), 1340.

Summers, D., Ma, C., 2000. A model for generating relativistic electrons in the earth's inner magnetosphere based on gyroresonant wave–particle interactions. Journal of Geophysical Research 105 (A2), 2625.

Summers, D., Thorne, R.M., Xiao, F., 1998. Relativistic theory of wave–particle resonant diffusion with application to electron acceleration in the magnetosphere. Journal of Geophysical Research 103 (A9), 20487.

Summers, D., Ma, C., Meredith, N.P., Horne, R.B., Thorne, R.M., Anderson, R.R., 2004. Modeling outer-zone relativistic electron response to whistler-mode chorus activity during substorms. Journal of Atmospheric and Solar-Terrestrial Physics 66, 133.

Summers, D., Ni, B., Meredith, N.P., 2007a. Timescales for radiation belt electron acceleration and loss due to resonant wave–particle interactions: 1. Theory. Journal of Geophysical Research 112 (A04206).

Summers, D., Ni, B., Meredith, N.P., 2007b. Timescales for radiation belt electron acceleration and loss due to resonant wave–particle interactions: 2. Evaluation for VLF chorus, ELF hiss, and electromagnetic ion cyclotron waves. Journal of Geophysical Research 112 (A04207).

Tsurutani, B.T., Gonzalez, W.D., 1987. The cause of high intensity long duration continuous AE activity (HILDCAA's): interplanetary Alfvén waves trains. Planetary and Space Science 35, 405.

Tsurutani, B.T., Gonzalez, W.D., 2007. A new perspective on the relationship between substorms and magnetic storms. Advances in Geosciences 8, 1.

Tsurutani, B.T., Gould, T., Goldstein, B.E., Gonzalez, W.D., Sugiura, M., 1990. Interplanetary Alfvén waves and auroral (substorm) activity: IMP-8. Journal of Geophysical Research 95, 2241.

Tsurutani, B.T., Ho, C.M., Smith, E.J., Neugebauer, M., Goldstein, B.E., Mok, J.S., Arballo, J.K., Balogh, A., Southwood, D.J., Feldman, W.C., 1994. The relationship between interplanetary discontinuities and Alfvén waves: Ulysses observations. Geophysical Research Letters 21, 2267.

Tsurutani, B.T., Gonzalez, W.D., Kamide, Y., Hoa, C.M., Lakhina, G.S., Arballo, J.K., Thorne, R.M., Pickett, J.S., Howard, R.A., 1999. The interplanetary causes of magnetic storms, HILDCAAs and viscous interaction. Physics and Chemistry of the Earth 24 (1–3), 93.

Tsurutani, B.T., Gonzalez, W.D., Guarnieri, F., Kamide, Y., Zhou, X., Arballo, J.K., 2004. Are high-intensity long-duration continuous AE activity (HILDCAA) events substorm expansion events? Journal of Atmospheric and Solar-Terrestrial Physics 66 (2), 167.

Tsurutani, B.T., Gonzalez, W.D., Gonzalez, A.L.C., Guarnieri, F.L., Gopalswamy, N., Grande, M., Kamide, Y., Kasahara, Y., Lu, G., Mann, I., McPherron, R., Søraas, F., Vasyliunas, V., 2006. Corotating solar wind streams and recurrent geomagnetic activity: a review. Journal of Geophysical Research 111 (A07S01).

Yahnin, A.G., Yahnina, T.A., Frey, H.U., 2007. Subauroral proton spots visualize the Pc1 source. Journal of Geophysical Research 112 (A10223).

Yahnina, T.A., Yahnin, A.G., Kangas, J., Manninen, J., 2000. Proton precipitation related to Pc1 pulsations. Geophysical Research Letters 27 (21), 3575.

Yahnina, T.A., Yahnin, A.G., Kangas, J., Manninen, J., 2002. Localized enhancements of energetic proton fluxes at low altitudes in the subauroral region and their relation to the pc1 pulsations. Cosmic Research 40 (3), 230.

Yahnina, T.A., Yahnin, A.G., Kangas, J., Manninen, J., Evans, D.S., Demekhov, A.G., Trakhtengerts, V.Y., Thomsen, M.F., Reeves, G.D., Gvozdevsky, B.B., 2003. Energetic particle counterparts for geomagnetic pulsations of Pc1 and IPDP types. Annales de Geophysique 21, 2281.